EDGE ARTICLE

Check for updates

Stepwise assembly of thiacalix[4]arene-protected Ag/Ti bimetallic nanoclusters: accurate identification of catalytic Ag sites in CO₂ electroreduction†

Yi-Qi Tian, Wen-Lei Mu, Lin-Lin Wu,* Xiao-Yi Yi, [ID] Jun Yan [ID] * and Chao Liu [ID] *

The accurate identification of catalytic sites in heterogeneous catalysts poses a significant challenge due to the intricate nature of controlling interfacial chemistry at the molecular level. In this study, we introduce a novel strategy to address this issue by utilizing a thiacalix[4]arene (TC4A)-protected Ti-oxo core as a template for loading Ag^{1+} ions, leading to the successful synthesis of a unique Ag/Ti bimetallic nanocluster denoted as Ti_8Ag_8. This nanocluster exhibits multiple surface-exposed Ag sites and possesses a distinctive "core–shell" structure, consisting of a $\{Ti_4@Ag_8(TC4A)_4\}$ core housing a $\{Ti_2O_2@Ag_4(TC4A)_2\}$ motif and two $\{Ti@Ag_2(TC4A)\}$ motifs. To enable a comprehensive analysis, we also prepared a Ti_2Ag_4 cluster with the same $\{Ti_2O_2@Ag_4(TC4A)_2\}$ structure found within Ti_8Ag_8. The structural disparities between Ti_8Ag_8 and Ti_2Ag_4 provide an excellent platform for a comparison of catalytic activity at different Ag sites. Remarkably, Ti_8Ag_8 exhibits exceptional performance in the electroreduction of CO_2 (eCO_2RR), showcasing a CO faradaic efficiency (FE_{CO}) of 92.33% at −0.9 V vs. RHE, surpassing the FE_{CO} of Ti_2Ag_4 (69.87% at −0.9 V vs. RHE) by a significant margin. Through density functional theory (DFT) calculations, we unveil the catalytic mechanism and further discover that Ag active sites located at $\{Ti@Ag_2(TC4A)\}$ possess a higher ε_d value compared to those at $\{Ti_2O_2@Ag_4(TC4A)_2\}$, enhancing the stabilization of the *COOH intermediate during the eCO_2RR. This study provides valuable insights into the accurate identification of catalytic sites in bimetallic nanoclusters and opens up promising avenues for efficient CO_2 reduction catalyst design.

Introduction

The electrochemical CO₂ reduction reaction (eCO₂RR) offers a promising approach for the conversion of CO₂ into valuable chemical fuels.[1,2] Ag-based nanomaterials have gained significant attention as electrocatalysts for the eCO₂RR, demonstrating remarkable selectivity towards CO generation.[3–6] Despite substantial advancements in the synthesis of monodisperse Ag nanoparticles with enhanced catalytic activity, their surface structures remain challenging to precisely characterize and define.[7,8] This limitation hinders the investigation of the structure–activity relationship. Consequently, it is crucial to attain synthetic control over the coordination environments of active Ag sites, enabling the creation of well-defined catalytic centers. Such control holds immense potential for elucidating the structure–activity relationship of Ag nanocatalysts, thereby facilitating efficient catalysis.

In the realm of Ag catalysis, pre-transition metal oxides (e.g., TiO₂) have gained significant prominence as substrates for the stabilization of Ag nanoparticles featuring surface-exposed catalytic sites.[9–13] The interplay between the oxide substrate and the active metal site manifests unique physical properties, thus prompting extensive investigations into the structural characteristics and reactive models of Ag–TiO₂ materials.[14] By establishing a close association between titanium-oxo clusters (TOCs) and TiO₂,[15–24] Ag-doped TOCs can be considered as molecular counterparts of bulk Ag–TiO₂ nanomaterials. Previous studies have successfully synthesized certain crystalline Ag–TOCs,[25–31] although the Ag sites were predominantly embedded within the TOCs as single atoms or clusters, impeding direct interaction with the reactants. Consequently, the controlled assembly of Ag–TOCs featuring surface-exposed Ag catalytic sites and the precise identification of their catalytic centers have posed significant challenges. Regarding the cluster assembly, ligands are the most important prerequisites that we should consider. Thiacalix[4]arene, a macrocyclic compound featuring four phenol units bridged by four S-

Hunan Provincial Key Laboratory of Chemical Power Sources, College of Chemistry and Chemical Engineering, Central South University, Changsha 410083, Hunan, P. R. China. E-mail: chaoliu@csu.edu.cn
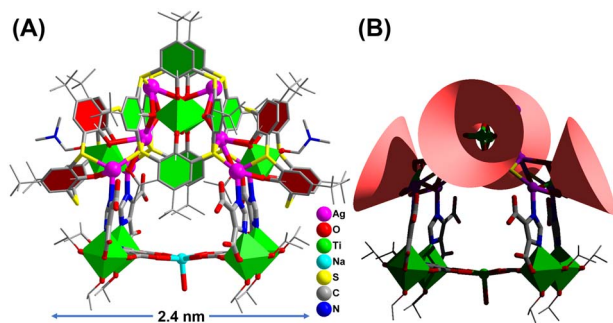
Fig. 1 Single-crystal X-ray structure of **Ti₈Ag₈**.

groups, has caught our attention, the oligomers of which are favourable to form typical tetranuclear M_4-TC4A units to fabricate high-nuclearity clusters.[32–37] According to soft and hard acid/base theory, the Ti^{4+} ion is a hard Lewis acid with a strong coordination affinity for phenolic oxygen, while Ag^{1+} is a soft Lewis acid that exhibits an affinity for soft bases, such as the S atom. It has here been assumed that if O-philic Ti^{4+} and S-philic Ag^{1+} ions participate in an assembly with TC4A, it would result in unexplored bimetallic clusters with unique geometric and/or electronic structures. Despite the existence of TC4A-protected TOCs[38–40] and Ag nanoclusters,[41–46] the synthesis of TC4A-stabilized Ag/Ti bimetallic clusters has yet to be reported in the literature.

Herein we provide a cluster model to accurately identify the Ag catalytic sites in CO_2 electroreduction. Through the synergistic assembly of TC4A and 4,5-imidazoledicarboxylic acid ($IdcH_2$), we synthesized the first calixarene-protected Ag^{1+}/Ti^{4+} bimetallic cluster of **Ti₈Ag₈** with the formula of [HNaTi₈Ag₈-O₂(TC4A)₄(HIdc)₆(ⁱPrO)₁₀(DMF)₂(H₂O)] (Fig. 1). The big cluster has a composite structure with two kinds of surface-exposed Ag sites, including the Ag(ɪ) sites in the two {Ti@Ag₂(TC4A)} and the Ag(ɪɪ) sites in the {Ti₂O₂@Ag₄(TC4A)₂} units. We have carefully studied the formation path of **Ti₈Ag₈** and crystallized four structural intermediates, **Ti₁Ag₁**, **Ti₂Ag₂**, **Ti₂Ag₂.₆** and **Ti₂Ag₄**, by controlling synthesis conditions. Interestingly, **Ti₂Ag₄** was exactly identical to the {Ti₂O₂@Ag₄(TC4A)₂} unit in **Ti₈Ag₈**, thus providing a perfect cluster model for comparing the catalytic activity of different Ag sites. The **Ti₈Ag₈** cluster was found to be an excellent eCO₂RR catalyst, which exhibited high reactivity and selectivity to CO (92.33% FE at −0.9 V vs. RHE), outperforming **Ti₂Ag₄**. The DFT method was used to calculate the free energy change of each elementary step in the conversion mechanism from CO_2 to CO, and in the competing hydrogen evolution reaction (HER). It was demonstrated that the Ag centers located on {Ti@Ag₂(TC4A)} could stabilize the *COOH intermediates in the CO_2 electroreduction better than those located on {Ti₂O₂@Ag₄(TC4A)₂}.

Results and discussion

Synthesis and characterization

The synthesis of **Ti₈Ag₈** was accomplished through a one-pot solvothermal reaction using $Ag(O_2CCF_3)$, $Ti(OⁱPr)_4$, TC4A, and

$IdcH_2$ in a 2 mL solution of ⁱPrOH/DMF (v/v = 1 : 2) at 80 °C for 2 days. This reaction yielded yellow prismatic crystals with a high yield of 60%. The composition of **Ti₈Ag₈** was determined using electrospray ionization-mass spectrometry (ESI-MS), which revealed a +2 signal at $m/z = 2663.46$, corresponding to the species [H₃NaTi₈Ag₈O₂(TC4A)₄(Idc)₆(ⁱPrO)₄]²⁺ (Fig. S33†). The molar ratio of Ti : Ag : Na in **Ti₈Ag₈** was determined through inductively coupled plasma (ICP) analysis (Table S2†), yielding a ratio of approximately 8 : 8 : 1, which is consistent with the findings from crystallography analysis. The geometrical structure of **Ti₈Ag₈** was found to be rather complicated, resembling a "hand basket", which can be divided into two parts. The handle of the basket is composed of a core–shell {Ti₄@Ag₈@(TC4A)₄} substructure (Fig. 2A), while the bottom of the basket is formed by one {Ti₄Na(Idc)₆} substructure (Fig. 2B). The {Ti₄@Ag₈(TC4A)₄} substructure can be further divided into two {Ti@Ag₂(TC4A)} motifs (Fig. 2C) and one {Ti₂O₂@Ag₄(TC4A)₂} motif (Fig. 2D). Upon inspecting the structure of {Ti₂O₂@Ag₄(TC4A)₂}, it was observed that each of the two completely deprotonated TC4A molecules accommodated an apical Ti^{4+} ion within their lower-rim tetraphenolic pocket, which are further fused together through two μ_2-O^{2-} to form {Ti₂O₂@(TC4A)₂} units. Additionally, the two Ti^{4+} ions inside the cage exhibited octahedral TiO_6 formations. The Ag4 array sandwiched between two calix entities formed a trapezium-like geometry. Among them, two exposed Ag(ɪ) sites (Ag1 and Ag2) were located in an O_3S_2 environment defined by two phenoxide, one μ_2-O^{2-}, and two S (Ag–S: 2.558(2)–2.589(2) Å and Ag–O: 2.499(2)–2.645(2) Å), while the Ag3 and Ag4 sites were fully coordinated and embedded within the cluster. In the {Ti@Ag₂(TC4A)} unit, TC4A accommodated the apical Ti^{4+} ion within its lower-rim tetraphenolic pocket, with two of the four S arms bridging to two Ag^{1+} ions. The four equivalent Ag(ɪɪ) sites (Ag5–Ag8) were in an O_2S_2N environment defined by two phenoxide (Ag–O: 2.696(9)–2.894(2) Å), two S (Ag–S: 2.487(2)–2.573(8) Å), and one imidazole N. The Ag–O bonds were relatively long, suggesting weaker interactions. One {Ti₂O₂@Ag₄(TC4A)₂} and two {Ti@Ag₂@TC4A} units were coupled together through four Ag–S bonds and six Ag–O bonds to form the {Ti₄@Ag₈@(TC4A)₄} substructure. In the {Ti₄Na(Idc)₆} substructure, the two Idc ligands at the bottom each bridged two Ti^{4+} ions to form two {Ti₂(Idc)} units, which were further bridged by a Na^+ ion to create a planar {Ti₄Na(Idc)₂} layer. The other four protonated Idc ligands acted as bridges between the {Ti@Ag₂TC4A} and {Ti₄-Na(Idc)₂} units. In this way, the two substructures of {Ti₄@Ag₈(-TC4A)₄} and {Ti₄Na(Idc)₆} were joined together by four Ag–N bonds (Ag–N: 2.220(5)–2.246(2) Å) to form the final **Ti₈Ag₈** cluster.

Tracking of the assembly process of Ti₈Ag₈

To understand the formation of **Ti₈Ag₈**, tracking its evolution process by mass spectrometry was performed. Firstly, the structural formation could be conveniently probed by matrix-assisted laser desorption/ionization time-of-flight mass spectrometry (MALDI-TOF-MS) of the crystalline samples of **Ti₈Ag₈** in the positive mode, using CH_2Cl_2 as a solvent (Fig. 3A). The pattern showed abundant fragment signals. The most dominant m/z peak at 1993.7 was attributed to the [HTi₂Ag₄O₂(TC4A)₂]¹⁺
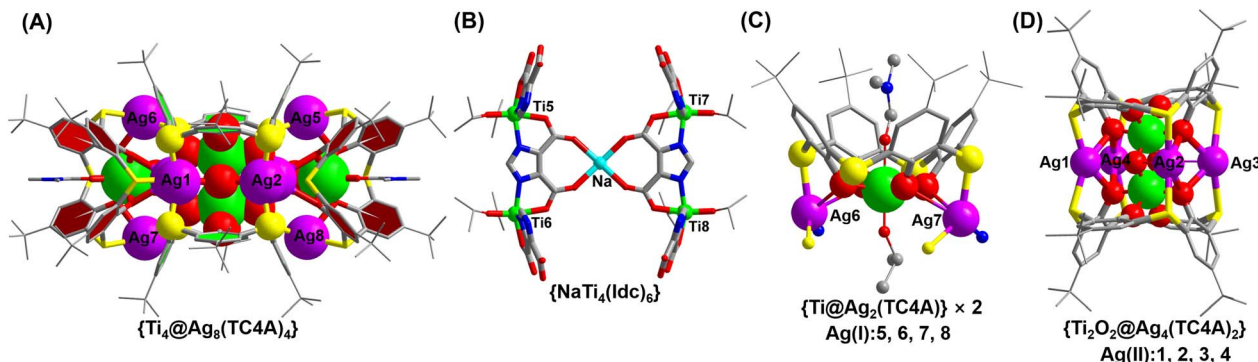
Fig. 2 Detailed local structures of $\{Ti_4@Ag_8(TC4A)_4\}$ (A), $\{Ti_4Na(Idc)_6\}$ (B), $\{Ti@Ag_2(TC4A)\}$ (C) and $\{Ti_2O_2@Ag_4(TC4A)_2\}$ (D).
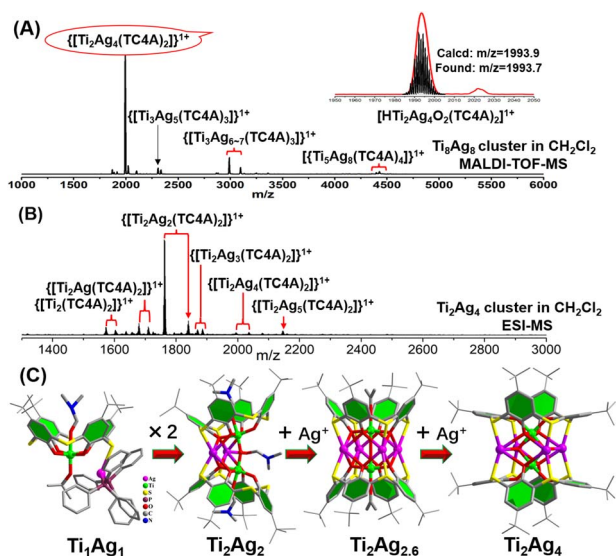
Fig. 3 (A) Positive-ion mode MALDI-TOF-MS of Ti_8Ag_8 dissolved in CH_2Cl_2. Inset: zoomed-in experimental and simulated ESI-MS of $[HTi_2Ag_4O_2(TC4A)_2]^{1+}$; (B) positive-ion mode ESI-MS of Ti_2Ag_4 dissolved in CH_2Cl_2. (C) Structures of the $TiAg$, Ti_2Ag_2, $Ti_2Ag_{2.6}$ and Ti_2Ag_4 clusters.

species, which corresponded to the $\{Ti_2O_2@Ag_4(TC4A)_2\}$ unit in Ti_8Ag_8. Interestingly, this intermediate could be crystallized and structurally resolved. The Ti_2Ag_4 cluster was synthesized by the reaction of TC4A and Ag(OAc) with $Ti(O^iPr)_4$ in CH_3CN/DMF. Structure determination revealed that the structure of Ti_2Ag_4 was exactly the same as that of the $\{Ti_2O_2@Ag_4(TC4A)_2\}$ unit in Ti_8Ag_8. This "core–shell" structure had a high chemical stability. One can see that only a peak corresponding to $[HTi_2Ag_4O_2(TC4A)_2]^{1+}$ was observed in the MALDI-TOF-MS of Ti_2Ag_4 in CH_2Cl_2, indicating that the cluster retained its integrity in solution (Fig. S35†). However, under the hard ionization conditions of ESI-MS, the pattern of Ti_2Ag_4 showed an abundance of cluster fragments (Fig. 3B). Signals corresponding to the units of $\{Ti_2@Ag_{4-x}(TC4A)_2\}$ ($x = 0$–4) can be found, which indicated that the four Ag^{1+} ions in Ti_2Ag_4 could be gradually dropped. The removal of Ag^{1+} ions indicated that the Ti_2Ag_4 cluster originated from the $\{Ti_2O_2@(TC4A)_2\}$ unit, whose surface abundance of S/O sites provided binding sites for the Ag^{1+} ions. The crystallography

data of structural intermediates Ti_1Ag_1, Ti_2Ag_2, and $Ti_2Ag_{2.6}$ help us precisely determine the structural model of the product generated upon fragmentation. These intermediates were all crystallized in the same system by a slight change in the reaction conditions. For Ti_1Ag_1, the TC4A unit kept one Ti^{4+} ion within the bowl, with one S arm binding to one $Ag(PPh_3)_2$ unit. For Ti_2Ag_2, two $\{Ti@TC4A\}$ units were bridged by one μ_2-O^{2-} ion and two Ag^{1+} ions, forming an asymmetrical semi-closed cage. $Ti_2Ag_{2.6}$ also contained a $\{Ti_2O@(TC4A)_2\}$ core, with a total number of 2.6 Ag^{1+} ions embedded in the waist in a disordered manner.

In the ESI-MS of Ti_2Ag_4, a distinctive signal corresponding to $[Na_2Ti_2Ag_5O_2(TC4A)_2]^{1+}$ was observed. This signal was formed by the binding of Ag^{1+} to the $\{Ti_2O_2@Ag_4(TC4A)_2\}$ core, suggesting that the $\{Ti_2O_2@Ag_4(TC4A)_2\}$ could serve as a seed for further growth. The primary question at this point was whether $\{Ti_2O_2@Ag_4(TC4A)_2\}$ could be further transformed into Ti_8Ag_8. Remarkably, the crystal of Ti_8Ag_8 can be directly obtained from the solvothermal reaction of Ti_2Ag_4, $Ti(O^iPr)_4$, and $IdcH_2$ in $^iPrOH/DMF$ at 80 °C for 2 days. Fig. 4 illustrates the time-dependent ESI-MS analysis of the mother liquor at different time intervals during the reaction. In the initial stage, the signals in the low m/z region closely resembled those observed in the ESI-MS of Ti_2Ag_4. However, as the reaction progressed, new signals emerged in the high m/z region. Specifically, peaks corresponding to the units of $[H_3NaTi_3Ag_8O_2(TC4A)_3(Idc)(^iPrO)_2(DMF)_2]^+$ ($m/z = 3633.70$) and $[HTi_4Ag_8O_2(TC4A)_4(OH)_2]^+$ ($m/z = 3988.76$) were detected at 4 hours and 8 hours, respectively. These fragments can be regarded as a combination of one $\{Ti_2O_2@Ag_4(TC4A)_2\}$ unit and one or two $\{Ti@Ag_2(TC4A)\}$ units. At the 24 hour mark, a +2 peak of $[H_3NaTi_6Ag_8O_2(TC4A)_4(HIdc)_5(^iPrO)_3]^{2+}$ ($m/z = 2500.30$) was observed, which is formed by the $\{Ti_4@Ag_8(TC4A)_4\}$ substructure bridging Ti^{4+} with Idc ligands. After 48 hours of reaction, the ESI-MS results of the mother liquid exhibited a series of +2 peaks within the m/z range of 2600–2900. Among them, the prominent peaks at 1 g and 1 h were assigned to $[H_3Na_2Ti_8Ag_8O_2(TC4A)_4(Idc)_6(^iPrO)_5(H_2O)_2]^{2+}$ and $[H_4NaTi_8Ag_8O_2(TC4A)_4(Idc)_6(^iPrO)_6(H_2O)]^{2+}$, respectively, confirming the formation of the Ti_8Ag_8 cluster. These findings clearly demonstrated that Ti_8Ag_8 could be derived from the $\{Ti_2O_2@Ag_4(TC4A)_2\}$ unit, following a small-to-large assembly pathway.

Thus, with the aid of the crystal structures of intermediate clusters, cluster fragment information, and growth paths
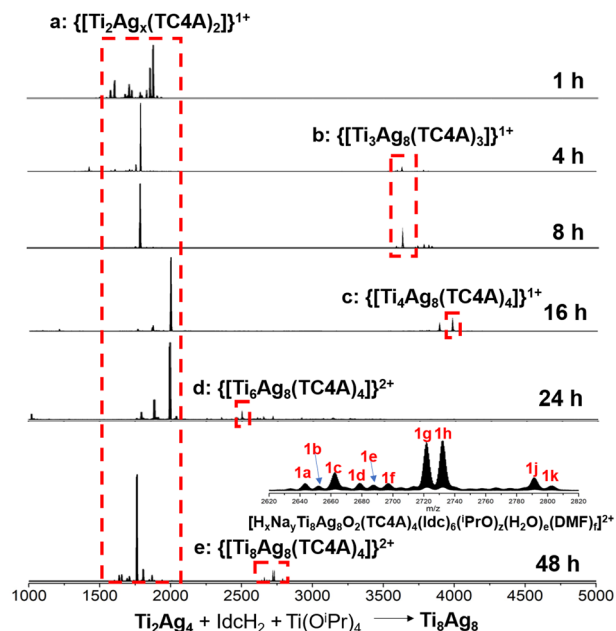
Fig. 4 Time-dependent ESI-MS in the range of m/z 1000–5000 for the reaction of Ti_2Ag_4, $Ti(O^iPr)_4$ and $IdcH_2$ in $^iPrOH/DMF$ at 80 °C at 1 h, 4 h, 8 h, 16 h, 24 h and 48 h.

revealed by time-dependent mass spectrometry, a comprehensive bottom-up evolution route for this series of TC4A-protected Ag/Ti bimetallic nanoclusters can be presented (Fig. S13†). In the initial stage, TC4A captures Ti^{4+} ions, leading to the formation of TOCs such as {Ti@(TC4A)} and {Ti$_2$O$_2$@(TC4A)$_2$}. The abundance of S/O sites on these TOCs enables them to act as substrates for the adsorption of Ag^{1+} ions, giving rise to the clusters of Ti_1Ag_1, Ti_2Ag_2, $Ti_2Ag_{2.6}$ and Ti_2Ag_4. These structures can be separated through crystallization under different conditions. Moving forward, the {Ti@Ag$_2$(TC4A)} and {Ti$_2$-O$_2$@Ag$_4$(TC4A)$_2$} units combine to form {Ti$_3$@Ag$_6$(TC4A)$_3$} and {Ti$_4$@Ag$_8$(TC4A)$_4$}. Subsequently, Ti^{4+} ions are bridged to the {Ti$_4$@Ag$_8$(TC4A)$_4$} substructure by the Idc^{2-} ligands, culminating in the formation of the final Ti_8Ag_8 cluster.

Electrochemical CO_2 reduction

Generally, the coordination and geometry environments to the Ag sites in Ag-based catalysts have an important effect on their catalytic activity. However, due to the lack of structural models, accurately comparing the catalytic activity of different Ag sites at the molecular level proves to be challenging. Upon detailed comparison of the XPS data for the clusters of Ti_2Ag_4 and Ti_8Ag_8, we observed a slight difference in the binding energies of the Ag species between them, with the binding energy of Ag in Ti_2Ag_4 approximately 0.1 eV lower compared to that of Ag in Ti_8Ag_8 (Fig. S26 and S27†). The subtle differences in their binding energies indicate variations in the local electronic structure and bonding characteristics between Ti_2Ag_4 and Ti_8Ag_8. Geometrically, the active Ag atoms in Ti_8Ag_8 could be divided into two nonequivalent groups: the four Ag(I) sites in two {Ti@Ag$_2$(TC4A)} and the two exposed Ag(II) sites in {Ti$_2$-O$_2$@Ag$_4$(TC4A)$_2$}. The structural differences between Ti_8Ag_8 and

Ti_2Ag_4 provided an ideal platform for an accurate comparison of eCO$_2$RR activities for those Ag sites.

The eCO$_2$RR activities of the Ti_8Ag_8 and Ti_2Ag_4 electrocatalysts were examined in a standard three-electrode configured H-type electrolytic cell with a 0.5 M KHCO$_3$ electrolyte. Linear sweep voltammetry (LSV) studies showed that Ti_8Ag_8 exhibited a much higher current density and a more positive onset potential in a CO_2 flow electrolyzer, as compared with an Ar purged one, indicating that Ti_8Ag_8 had CO_2 reduction activity (Fig. 5A). The cyclic voltammetry (CV) studies of Ti_8Ag_8 in a proton-deficient organic solution showed similar results (Fig. S41†). For comparison, the LSV of Ti_2Ag_4 exhibits much lower current density. Fig. 5B compares the FE of the CO formation for the two clusters. Only CO and H$_2$ were detected by gas chromatography. No other liquid product had been formed according to the ^1H NMR spectra. Ti_8Ag_8 exhibited a higher FE$_{CO}$ than Ti_2Ag_4 over the selected potential range from −0.6 V to −1.2 V. It achieved the maximum FE$_{CO}$ of 92.33% at −0.9 V, which was much higher than the corresponding value of 69.87% for Ti_2Ag_4. The CO partial current density (J_{CO}) for the two clusters was also calculated (Fig. 5C), and the J_{CO} of Ti_8Ag_8 reached 23.46 mA cm^{-2} at −1.2 V $vs.$ RHE, which was at least 2.5 times larger than that of Ti_2Ag_4 (9.50 mA cm^{-2}). This indicates an improved catalytic activity and selectivity of Ti_8Ag_8 for the electrocatalytic CO_2RR.

To find the underlying reasons for the performance differences between the two clusters, the Tafel slope was used to characterize their reaction kinetics in the electrolyte. The Tafel slope of Ti_8Ag_8 was found to be smaller than that of Ti_2Ag_4, indicating that Ti_8Ag_8 had more favorable reaction kinetics of CO formation, which may be due to the more efficient charge transfer and larger active surface of Ti_8Ag_8 during the catalytic
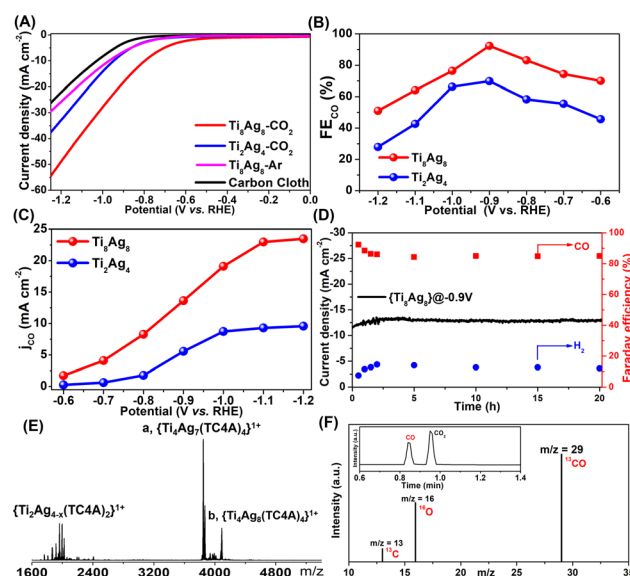

Fig. 5 (A) LSV curves in CO_2-saturated 0.5 M KHCO$_3$ solution; (B) the FE$_{CO}$ values at different applied potentials in CO_2-saturated 0.5 M KHCO$_3$ solution; (C) the CO partial current density (J_{CO}); (D) stability tests of the electrocatalysts for CO_2 reduction; (E) ESI-MS of Ti_8Ag_8 electrocatalysts after reaction; (F) GC-MS of ^{13}CO recorded under a $^{13}CO_2$ atmosphere.

process (Fig. S45†). To verify this, the electrochemically active surface area (ECSA) was characterized (Fig. S46†). By plotting $\Delta J/2 = (J_a - J_c)/2$ at -0.12 V *vs.* RHE against the scan rate, the calculated electrochemical C_{dl} of **Ti₈Ag₈** is 6.18 mF cm^{-2}, higher than that of **Ti₂Ag₄** (5.54 mF cm^{-2}), which indicated that **Ti₈Ag₈** had a faster reaction speed in the CO₂RR process and had more active sites to contact with electrolyte.

The electrochemical stability of **Ti₈Ag₈** was evaluated with chronopotentiometry at -0.9 V *vs.* RHE. The current density and FE$_{CO}$ kept almost stable during 20 h continuous electrolysis, indicative of the excellent reaction stability of **Ti₈Ag₈** (Fig. 5D). We also recovered the catalyst after the reaction and conducted ESI-MS measurements. The ESI-MS pattern showed two strong signals that corresponded to [HTi₄Ag₈O₂(TC4A)₄(-^{i}PrO)₂(H₂O)]$^{1+}$ and [H₂Ti₄Ag₇O₂(TC4A)₄]$^{1+}$. This indicated that the core structure of {Ti₄@Ag₈(TC4A)₄} was still stable (Fig. 5E). Additionally, EDS analysis of the catalyst after the reaction indicated that the Ti and Ag elements remained in a 1 : 1 ratio (Fig. S50†). XPS analysis showed no significant change in the binding energy of the Ag element in the catalyst before and after the reaction, signifying the preservation of its coordination environment (Fig. S51†). Transmission electron microscopy (TEM) revealed the presence of clusters in the solution as discrete particles, with an average particle size of approximately 3 nanometers, consistent with the cluster size measured by SCXRD, further confirming the stability of the catalyst (Fig. S52†). To further determine the C origin of the products, an isotopic experiment was performed under similar catalytic conditions, but by using ^{13}CO₂ as the C source. The production of ^{13}CO ($m/z = 29$) was then studied by using GC-MS, which showed that the generated CO came from CO₂ (Fig. 5F).

DFT calculations were performed to investigate the reactivity of the two clusters. The calculation models, **Ti₄Ag₈_m** and **Ti₂Ag₄_m**, were optimized based on the crystal structures, by simplifying ^{t}Bu groups of benzene rings to H atoms and ^{i}PrO groups to MeO groups. In addition, the Ti₄Na(Idc)₆ groups in **Ti₈Ag₈** were removed to create active sites to build **Ti₄Ag₈_m**. The Gibbs free energy diagrams of the CO₂RR and HER are shown in Fig. 6. The proposed pathway for the CO₂ reduction to CO was CO₂(g) → *COOH → *CO → CO(g). The calculated Gibbs free energies of the CO₂RR revealed that the formation of *COOH was the rate determining step. The Gibbs free energy that was calculated for the formation of *COOH on the Ag site on the {Ti@Ag₂(TC4A)} unit in **Ti₄Ag₈_m** was 1.01 eV, which was much lower than the corresponding Gibbs free energy for the {Ti@Ag₂(TC4A)} unit in **Ti₂Ag₄_m** (1.42 eV). This result suggested that the Ag sites on {Ti@Ag₂(TC4A)} were more energetically favorable for the catalysis of the CO₂ conversion to CO than those on {Ti₂O₂@Ag₄(TC4A)₂}. The Gibbs free energies of the adsorptions were also calculated to illustrate the HER reactivities of **Ti₈Ag₈** and **Ti₂Ag₄**. The high Gibbs free energies of the H* adsorption revealed that both **Ti₈Ag₈** (1.63 eV) and **Ti₂Ag₄** (2.00 eV) were unfavorable in the formation of H₂. By comparing the Gibbs free energy diagrams of the CO₂RR and HER, we found that **Ti₄Ag₈_m** had a higher selectivity for the CO formation, as compared with **Ti₂Ag₄_m**.
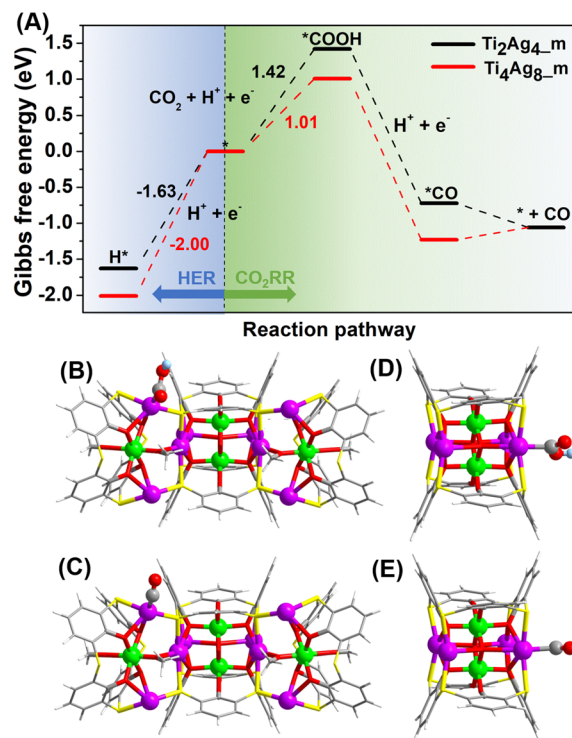

Fig. 6 (A) Free energy diagrams for the CO₂RR and HER on **Ti₄Ag₈_m** (red) and **Ti₂Ag₄_m** (black); the calculation optimized structures of COOH absorbed on **Ti₄Ag₈_m** (B) and **Ti₂Ag₄_m** (C); the calculation optimized structures of CO absorbed on **Ti₄Ag₈_m** (D) and **Ti₂Ag₄_m** (E).

To further unravel the mystery of the differences in catalytic performances, the d-band center (ε_d) of the Ag sites in **Ti₄Ag₈_m** and **Ti₂Ag₄_m** was calculated to evaluate their reactivity as active sites, since ε_d has been proposed as a benchmark descriptor for transition metal reactivity.[47] Our calculations showed markedly different electronic properties for the two nonequivalent Ag sites (Fig. S53†). In **Ti₄Ag₈_m**, the ε_d value of the four Ag(ɪ) sites in {Ti@Ag₂(TC4A)} is -0.34 eV, which is 0.06 eV higher than that of the two surface-exposed Ag(ɪɪ) sites in {Ti₂O₂@Ag₄(TC4A)₂}. As a comparison, the four Ag(ɪɪ) sites in **Ti₂Ag₄_m** also exhibit a lower ε_d value of -0.44 eV, suggesting that the Ag(ɪ) sites in {Ti@Ag₂(TC4A)} are more active than Ag(ɪɪ) in the {Ti₂O₂@Ag₄(-TC4A)₂} unit. Furthermore, the projected density of states (PDOS) showed that the active Ag(ɪ) sites in **Ti₄Ag₈_m** underwent a stronger hybridization with the absorbed COOH and CO than those in **Ti₂Ag₄_m** (Fig. S55†). It is important to stress that the results from the DFT calculations were consistent with the corresponding experimental results. The combined theoretical and experimental investigations have thereby resulted in a fundamental understanding of the CO₂RR mechanism involving different Ag active sites on the Ag/Ti bimetallic clusters.

Conclusions

In summary, we have for the first time compared eCO₂RR atomic-level activities for different Ag sites on Ag-based catalysts. We synthesized and characterized an atomically precise

bimetallic **Ti₈Ag₈** cluster using a calixarene-protected Ti-oxo core as a substrate for loading Ag^{1+} ions. The **Ti₈Ag₈** clusters contain two groups of surface-exposed Ag catalytic sites, located on the {Ti$_2$O$_2$@Ag$_4$(TC4A)$_2$} and {Ti@Ag$_2$(TC4A)} units, respectively. We traced the assembly path of **Ti₈Ag₈** and successfully isolated {Ti$_2$O$_2$@Ag$_4$(TC4A)$_2$} in the **Ti₂Ag₄** cluster alone. The eCO$_2$RR test showed that both clusters were good electrocatalysts for the reduction of CO$_2$ to CO, but the performance of **Ti₈Ag₈** was significantly superior to that of **Ti₂Ag₄**. Also, DFT was used to calculate the free energy change of each elementary step for converting CO$_2$ into CO and the competing HER, revealing the difference in activity between the Ag sites on the {Ti@Ag$_2$(TC4A)} and {Ti$_2$O$_2$@Ag$_4$(TC4A)$_2$} units. This work clearly demonstrated that subtle changes in the coordination geometry of catalytic sites can greatly affect the catalytic performance; thus, the attainment of the atomic structures of nanoclusters is of critical importance, which could provide a valuable reference for rational design of cluster structures to achieve efficient catalysis.

Data availability

The data that support the findings of this study are available in the main text and the ESI.†

Author contributions

C. L. and J. Y. supervised the project and conceived the idea. Y. Q. T. carried out synthesis, characterization and electrochemical experiments of clusters. C. L. and Y. Q. T. wrote the manuscript. L. L. W. undertook the calculations for this article. All authors discussed the experimental results.

Conflicts of interest

There are no conflicts of interest to declare.

Acknowledgements

Notes and references

1 J. A. Turner, *Science*, 1999, **285**, 687–689.
2 P. De Luna, C. Hahn, D. Higgins, S. A. Jaffer, T. F. Jaramillo and E. H. Sargent, *Science*, 2019, **364**, 350–359.
3 G. Wang, J. Chen, Y. Ding, P. Cai, L. Yi, Y. Li, C. Tu, Y. Hou, Z. Wen and L. Dai, *Chem. Soc. Rev.*, 2021, **50**, 4993–5061.
4 L. Qin, F. Sun, X. Ma, G. Ma, Y. Tang, L. Wang, Q. Tang, R. Jin and Z. Tang, *Angew. Chem., Int. Ed.*, 2021, **60**, 26136–26141.
5 J. Y. Xu, L. Xiong, X. Cai, S. S. Tang, A. C. Tang, X. Liu, Y. Pei and Y. Zhu, *Chem. Sci.*, 2022, **13**, 2778–2782.
6 J. Wang, F. Xu, Z.-Y. Wang, S.-Q. Zang and T. C. W. Mak, *Angew. Chem., Int. Ed.*, 2022, **61**, e202207492.
7 I. Chakraborty and T. Pradeep, *Chem. Rev.*, 2017, **117**, 8208–8271.
8 R. Jin, C. Zeng, M. Zhou and Y. Chen, *Chem. Rev.*, 2016, **116**, 10346–10413.
9 P. Liu, Y. Zhao, R. Qin, S. Mo, G. Chen, L. Gu, D. M. Chevrier, P. Zhang, Q. Guo, D. Zang, B. Wu, G. Fu and N. Zheng, *Science*, 2016, **352**, 797–800.
10 J. Wan, W. Chen, C. Jia, L. Zheng, J. Dong, X. Zheng, Y. Wang, W. Yan, C. Chen, Q. Peng, D. Wang and Y. Li, *Adv. Mater.*, 2018, **30**, 1705369.
11 L. DeRita, S. Dai, K. L. Zepeda, N. Pham, G. W. Graham, X. Pan and P. Christopher, *J. Am. Chem. Soc.*, 2017, **139**, 14150–14165.
12 H. Guan, J. Lin, B. Qiao, X. Yang, L. Li, S. Miao, J. Liu, A. Wang, X. Wang and T. Zhang, *Angew. Chem., Int. Ed.*, 2016, **55**, 2820–2824.
13 W. N. Wang, W. J. An, B. Ramalingam, S. Mukherjee, D. M. Niedzwiedzki, S. Gangopadhyay and P. Biswas, *J. Am. Chem. Soc.*, 2012, **134**, 11276–11281.
14 S. Chen, Z. N. Chen, W. H. Fang, W. Zhuang, L. Zhang and J. Zhang, *Angew. Chem., Int. Ed.*, 2019, **58**, 10932–10935.
15 P. Coppens, Y. Chen and E. Trzop, *Chem. Rev.*, 2014, **114**, 9645–9661.
16 W. H. Fang, L. Zhang and J. Zhang, *Chem. Soc. Rev.*, 2018, **47**, 404–421.
17 L. Rozes and C. Sanchez, *Chem. Soc. Rev.*, 2011, **40**, 1006–1030.
18 P. D. Matthews, T. C. King and D. S. Wright, *Chem. Commun.*, 2014, **50**, 12815–12823.
19 Y. Lv, J. Cheng, A. Steiner, L. Gan and D. S. Wright, *Angew. Chem., Int. Ed.*, 2014, **53**, 1934–1938.
20 C. Zhao, Y. Z. Han, S. Dai, X. Chen, J. Yan, W. Zhang, H. Su, S. Lin, Z. Tang, B. K. Teo and N. Zheng, *Angew. Chem., Int. Ed.*, 2017, **56**, 16252–16256.
21 G. Zhang, C. Liu, D. L. Long, L. Cronin, C. H. Tung and Y. Wang, *J. Am. Chem. Soc.*, 2016, **138**, 11097–11100.
22 W. H. Fang, L. Zhang and J. Zhang, *J. Am. Chem. Soc.*, 2016, **138**, 7480–7483.
23 M. Y. Gao, F. Wang, Z. G. Gu, D. X. Zhang, L. Zhang and J. Zhang, *J. Am. Chem. Soc.*, 2016, **138**, 2556–2559.
24 J. X. Liu, M. Y. Gao, W. H. Fang, L. Zhang and J. Zhang, *Angew. Chem., Int. Ed.*, 2016, **55**, 5160–5165.
25 S. Chen, W.-H. Fang, L. Zhang and J. Zhang, *Angew. Chem., Int. Ed.*, 2018, **57**, 11252–11256.
26 X. Fan, F. Yuan, D. Li, S. Chen, Z. Cheng, Z. Zhang, S. Xiang, S.-Q. Zang, J. Zhang and L. Zhang, *Angew. Chem., Int. Ed.*, 2021, **60**, 12949–12954.
27 G. H. Chen, D. J. Li, Y. P. He, S. H. Zhang, F. P. Liang and J. Zhang, *Inorg. Chem.*, 2020, **59**, 14861–14865.
28 X. M. Luo, C. H. Gong, X. Y. Dong, L. Zhang and S. Q. Zang, *Nano Res.*, 2021, **14**, 2309–2313.

29 Y. Z. Yu, Y. Guo, Y. R. Zhang, M. M. Liu, Y. R. Feng, C. H. Geng and X. M. Zhang, *Dalton Trans.*, 2019, **48**, 13423–13429.

30 Y. J. Liu, P. Shao, M. Y. Gao, W. H. Fang and J. Zhang, *Inorg. Chem.*, 2020, **59**, 11442–11448.

31 M. Y. Gao, K. Wang, Y. Y. Sun, D. J. Li, B. Q. Song, Y. H. Andaloussi, M. J. Zaworotko, J. Zhang and L. Zhang, *J. Am. Chem. Soc.*, 2020, **142**, 12784–12790.

32 M. M. Deegan, T. S. Ahmed, G. P. A. Yap and E. D. Bloch, *Chem. Sci.*, 2020, **11**, 5273–5279.

33 H. T. Han, L. Kan, P. Li, G. S. Zhang, K. Y. Li, W. P. Liao, Y. L. Liu, W. Chen and C. H. T. Hu, *Sci. China: Chem.*, 2021, **64**, 426–431.

34 D. T. Geng, X. Han, Y. F. Bi, Y. C. Qin, Q. Li, L. L. Huang, K. Zhou, L. J. Song and Z. P. Zheng, *Chem. Sci.*, 2018, **9**, 8535–8541.

35 M. Liu, W. P. Liao, C. Hu, S. C. Du and H. J. Zhang, *Angew. Chem., Int. Ed.*, 2012, **51**, 1585–1588.

36 X. X. Hang, B. Liu, X. F. Zhu, S. T. Wang, H. T. Han, W. P. Liao, Y. L. Liu and C. H. Hu, *J. Am. Chem. Soc.*, 2016, **138**, 2969–2972.

37 S. T. Wang, X. H. Gao, X. X. Hang, X. F. Zhu, H. T. Han, X. K. Li, W. P. Liao and W. Chen, *J. Am. Chem. Soc.*, 2018, **140**, 6271–6277.

38 X. Wang, Y. N. Yu, Z. Wang, J. Zheng, Y. F. Bi and Z. P. Zheng, *Inorg. Chem.*, 2020, **59**, 7150–7157.

39 Y. Q. Tian, Y. S. Cui, J. H. Zhu, C. Q. Xu, X. Y. Yi, J. Li and C. Liu, *Chem. Commun.*, 2022, **58**, 9034–9037.

40 Y. Q. Tian, Y. S. Cui, W. D. Yu, C. Q. Xu, X. Y. Yi, J. Yan, J. Li and C. Liu, *Chem. Commun.*, 2022, **58**, 6028–6031.

41 Z. Wang, L. Li, L. Feng, Z. Y. Gao, C. H. Tung, L. S. Zheng and D. Sun, *Angew. Chem., Int. Ed.*, 2022, **61**, e202200823.

42 Z. Wang, H. F. Su, Y. W. Gong, Q. P. Qu, Y. F. Bi, C. H. Tung, D. Sun and L. S. Zheng, *Nat. Commun.*, 2020, **11**, 308.

43 Z. Wang, F. Alkan, C. M. Aikens, M. Kurmoo, Z. Y. Zhang, K. P. Song, C. H. Tung and D. Sun, *Angew. Chem., Int. Ed.*, 2022, **61**, e202206742.

44 S. Q. Li, L. F. Dai, Y. Q. Tian, Y. X. Yi, J. Yan and C. Liu, *Chem. Commun.*, 2023, **59**, 575–578.

45 Z. J. Guan, J. L. Zeng, Z. A. Nan, X. K. Wan, Y. M. Lin and Q. M. Wang, *Sci. Adv.*, 2016, **2**, e1600323.

46 Z. J. Guan, F. Hu, S. F. Yuan, Z. A. Nan, Y. M. Lin and Q. M. Wang, *Chem. Sci.*, 2019, **10**, 3360–3365.

47 J. K. Nørskov, T. Bligaard, J. Rossmeisl and C. H. Christensen, *Nat. Chem.*, 2009, **1**, 37–46.